# Added Masses of generic shape bodies interacting with external walls

Giovanni Carbone, Guillaume Martinat, Dominique Farcy, Jean-Luc Harion

# Added Masses of generic shape bodies interacting with external walls

Giovanni Carbone[a,b,c,*], Guillaume Martinat[a], Dominique Farcy[b], Jean-Luc Harion[c]

[a] *FLYING WHALES, 13-17, rue Pages, 92150 Suresnes, France*
[b] *ONERA The French Aerospace Lab, 5 rue des Fortifications, 59045 Lille, France*
[c] *IMT Lille Douai, 764, Boulevard Lahure, 59508 Douai, France*

**Abstract**

The aim of this paper is to propose an efficient method to evaluate the Added Masses of generic shape bodies in infinite fluid or in the proximity of external walls. The Added Masses (AM) are the result of the inertial reaction of the fluid in response to an accelerated movement of a body immersed in it. The AM effects are more evident when the body density is similar to that of the surrounding fluid, as in the case of airships. In the take-off or landing phases, the proximity to the ground causes an increase in the Added Masses that must be correctly estimated to properly size the airship controls. In our method, the calculation of the Added Masses matrix is carried out by the Boundary Element Method (BEM). To verify the accuracy of the results, the study cases are based on simple shapes, whose Added Masses are well known. The analyses in infinite fluid and in the presence of a flat wall are carried out. Numerical results are compared to the theoretical values found in literature. The calculated Added Masses are intrinsically dependent on the mesh definition and the relative error, referred to the theoretical values, depends on the surface and volume discretization. In the case of interaction between geometries with complex shapes, the influence on the Added Masses is very difficult to predict without a numerical approach. The method proposed gives a good compromise in terms of quality

*Corresponding author
*Email address:* giovanni.carbone@flying-whales.com (Giovanni Carbone)

of results and computational cost.

*Keywords:* Added Masses, Boundary Element Method, External Wall Interaction, Airships

## 1. Introduction

Airships represent the frontier of the future regarding the air transport sector. These vehicles, widely used in the past, are finding more interest in our days thanks to their potential in many applications, such as the transport of heavy materials in landlocked areas, which distinguish them as unique in their kind.

The airships dynamics is very different from that of the most common aircraft because of the impact of the Added Masses (AM) effects. The concept of AM was introduced for the first time by Pierre Louis George, comte du Buat [1]. The accelerated motion of a body immersed in a fluid induces a variation on the kinetic energy of the latest. The additional work done by the body to balance this effect, in the vacuum would be equivalent to the work needed to accelerate an additional inertia.

AM are directly proportional to the fluid density, so their effects are not negligible when the density of the body is comparable to that of the surrounding fluid. Their estimation is fundamental during the design phase of an airship, to evaluate the aerodynamic loads and to dimension the structure, the propulsion and control systems. Analytical expressions of AM evaluated on a sphere and on ellipsoidal shapes placed in infinite fluid, were obtained by Lamb [2]. Studies on the interaction of a sphere with a flat wall were realized by Hicks [3], who obtained an analytical formulation of the AM variations when the body is moving in the orthogonal direction to the wall, with the development of the Image Method. A solution for the case of motion in the parallel direction to the wall was proposed by Davis [4]. Kharlamov [5] solved the two problems by a successive-image method. More realistic shapes of airships were studied by Azouz [6], that presented an analytical method for the calculation of the AM,

based on the integration of elliptic sections. The Boundary Element Method (BEM), described in [7, 8], was applied by Ceruti [9], Tuveri [10] and Ghassemi [11] to solve the Laplace equation and to evaluate the Added Masses on bodies with complex geometries immersed in infinite fluid. In [12] is proposed a method to optimize the external shape of a hybrid airship by a direct evaluation of the Added Masses. The take-off case is analyzed, but no corrections on the Added Masses values as a function of the distance from the ground are considered.

All the flight phases in the proximity of the ground are the most delicate and critical for an airship. For this reason, the purpose of this study is to have a better understanding of the AM variations in the presence of nearby walls. The BEM is developed to analyze the Added Masses in more realistic environments, studying the interaction of a body with generic external walls.

This paper is organized as follows: in Section 2, a summary of the Added Masses theory and of the numerical method adopted for our calculations is provided. In Section 3 are presented the results obtained on the analysis of a sphere, of ellipsoids and of an airship shape.

## 2. Methodology

### *2.1. Added Masses Theory*

For a non-deformable body immersed in a stationary inviscid fluid, the terms of the 6-by-6 Added Masses matrix, indexed by $i$ and $j$, are defined as:

$$\lambda_{ij} = -\rho \iint_S \frac{\partial \varphi_i}{\partial \vec{n}} \varphi_j \, dS \tag{1}$$

$S$ and $\vec{n}$ respectively indicate the body surface and the normal vector to the surface, $\rho$ is the density of the fluid and $\varphi_i$ represents an elementary velocity potential. With a linear combination of $\varphi_i$, the velocity potential of the fluid can be written as:

$$\varphi = u_x\varphi_1 + u_y\varphi_2 + u_z\varphi_3 + \omega_x\varphi_4 + \omega_y\varphi_5 + \omega_z\varphi_6 \tag{2}$$

where $u_j$ and $\omega_j$ (with $j = x, y, z$) represent the body linear and angular velocities projected along three orthogonal directions of a reference frame placed on the body center of volume.

On the body surface, the velocity of the fluid is equal to:

$$\begin{aligned}\left.\frac{\partial\varphi}{\partial\vec{n}}\right|_S &= u_n = u_x\alpha + u_y\beta + u_z\gamma \\ &= u_{0x}\alpha + u_{0y}\beta + u_{0z}\gamma + \omega_x(d_y\gamma - d_z\beta) + \omega_y(d_z\alpha - d_x\gamma) + \omega_z(d_x\beta - d_y\alpha)\end{aligned} \tag{3}$$

where $\alpha$, $\beta$ and $\gamma$ are the direction cosines measured between the normal vectors and the axes of the reference frame, equal to $\cos(\vec{n},\vec{x})$, $\cos(\vec{n},\vec{y})$ and $\cos(\vec{n},\vec{z})$. The coordinates of a point on the surface $S$, referred to the origin of the body-fixed reference frame, are indicated by $d_x$, $d_y$ and $d_z$.

Knowing that each elementary potential $\varphi_i$ is a solution of the Laplace problem,

$$\Delta\varphi_i = 0 \tag{4}$$

it is possible to deduce the boundary conditions of this equation from Eq. 2 and Eq. 3, and from the stationarity condition at infinity:

$$\left.\frac{\partial\varphi_i}{\partial\vec{n}}\right|_S = \begin{cases} \alpha & i = 1 \\ \beta & i = 2 \\ \gamma & i = 3 \\ d_y\gamma - d_z\beta & i = 4 \\ d_z\alpha - d_x\gamma & i = 5 \\ d_x\beta - d_y\alpha & i = 6 \end{cases} \qquad \text{and} \qquad \lim_{d\to\infty}\frac{\partial\varphi_i}{\partial x} = \lim_{d\to\infty}\frac{\partial\varphi_i}{\partial y} = \lim_{d\to\infty}\frac{\partial\varphi_i}{\partial z} = 0 \tag{5}$$

According to Eq. 1, it is possible to evaluate the Added Masses matrix of a generic body by solving the six Laplace equations and finding $\varphi_i$ on each point of the body surface $S$.

*2.2. Numerical Method*

In order to solve Eq. 4 numerically, the Boundary Element Method is adopted. The velocity potential of each point of the field can be expressed as an integral equation, corresponding to a distribution of sources and dipoles. Therefore, a generic velocity potential $\phi$, evaluated on a point $P$ of the body surface, can be defined as:

$$\phi(P) = \iint_S \frac{\phi(Q)}{2\pi} \frac{\partial G}{\partial \vec{n}} \, dS - \iint_S \frac{\partial \phi(Q)}{\partial \vec{n}} \frac{G}{2\pi} \, dS \tag{6}$$

where $G$ is the Green function. In a three-dimensional case $G$ can be expressed with $G = \frac{1}{\|\vec{r}\|}$, where $\vec{r}$ is the distance between the point $P$ and another generic point $Q$, associated to the surface element $dS$. Discretizing Eq. 6, a linear system of algebraic equations of the unknown $\phi$ is obtained (the indices $i$ and $j$ refer to different surface points):

$$\phi_i = \sum_{j=1}^{N_b} \phi_j \frac{C_{ij}}{2\pi} - \sum_{j=1}^{N_b} \frac{\partial \phi_j}{\partial \vec{n}} \frac{B_{ij}}{2\pi} \tag{7}$$

in which

$$C_{ij} = \frac{\partial}{\partial \vec{n}_j} \left( \frac{1}{\|\vec{r}_{ij}\|} \right) \delta S_j \tag{8}$$

$$B_{ij} = \frac{1}{\|\vec{r}_{ij}\|} \, \delta S_j \tag{9}$$

and $N_b$ is the number of discretization elements of the surface. Eq. 7 can be rewritten in matrix form:

$$[2\pi \mathbb{I} - C]_{N_b \times N_b} \{\phi\}_{N_b \times 1} = -[B]_{N_b \times N_b} \left\{ \left. \frac{\partial \phi}{\partial \vec{n}} \right|_S \right\}_{N_b \times 1} \tag{10}$$

with $\mathbb{I}$ the $N_b$-by-$N_b$ identity matrix. Replacing in Eq. 10 one of the six $\varphi_i$ and the corresponding boundary conditions $\left. \frac{\partial \varphi_i}{\partial \vec{n}} \right|_S$ described in Eq. 5, it is possible to evaluate the elementary potentials on each point of the surface. The computation of the Added Masses matrix is obtained with a discretization of Eq. 1:

$$\mathbb{M}_a = -\rho \begin{bmatrix} \sum_{i=1}^{N_b} (\varphi_1)_i \left( \left. \frac{\partial \varphi_1}{\partial \vec{n}} \right|_S \right)_i dS_i & \dots & \sum_{i=1}^{N_b} (\varphi_1)_i \left( \left. \frac{\partial \varphi_6}{\partial \vec{n}} \right|_S \right)_i dS_i \\ \dots & \ddots & \dots \\ \sum_{i=1}^{N_b} (\varphi_6)_i \left( \left. \frac{\partial \varphi_1}{\partial \vec{n}} \right|_S \right)_i dS_i & \dots & \sum_{i=1}^{N_b} (\varphi_6)_i \left( \left. \frac{\partial \varphi_6}{\partial \vec{n}} \right|_S \right)_i dS_i \end{bmatrix} \tag{11}$$

*2.3. Singular points*

In the numerical method presented in the previous section, the presence of singular points is observed in Eq. 8 and Eq. 9 when $i = j$, because of $\|\vec{r}_{ij}\| = 0$.

The strategy adopted to solve this numerical problem consists in a further discretization of each element of the mesh, divided into $k$ sub-elements, as shown in Figure 2 and considering the distance between the centroid of the $i$ element and the centroid of all relative $k$ sub-elements. The distance $\|\vec{r}_{iik}\|$, that is always greater than zero, because the centroid of each $k$ sub-elements cannot coincide with the centroid of the $i$ element, is employed to evaluate the $k$ contribution to $C_{ii}$ and $B_{ii}$, in Eq. 8 and Eq. 9, by the following equations:

$$C_{iik} = -\frac{\vec{r}_{iik} \cdot \vec{n}_i}{\|\vec{r}_{iik}\|^3} \delta S_{ik} = 0 \tag{12}$$

$$B_{iik} = \frac{1}{\|\vec{r}_{iik}\|} \delta S_{ik} \tag{13}$$

The final value of $C_{ii}$ and $B_{ii}$ is calculated by the sum of the $k$ contributions $C_{iik}$ and $B_{iik}$.

In order to increase the quality of the results, the method is not only applied to the $i = j$ case, but also to the rest of the domain. So Eq. 7, Eq. 8 and Eq. 9 are rewritten as:

$$\phi_i = \sum_{j=1}^{N_b} \phi_j \sum_{k=1}^{N_{sub}} \frac{C_{ijk}}{2\pi} - \sum_{j=1}^{N_b} \frac{\partial \phi_j}{\partial \vec{n}} \sum_{k=1}^{N_{sub}} \frac{B_{ijk}}{2\pi} \tag{14}$$

$$C_{ijk} = -\frac{\vec{r}_{ijk} \cdot \vec{n}_j}{\|\vec{r}_{ijk}\|^3} \delta S_{jk} \tag{15}$$

$$B_{ijk} = \frac{1}{\|\vec{r}_{ijk}\|} \delta S_{jk} \tag{16}$$

where $\vec{r}_{ijk}$ is the distance from the center of the $i$ element and the center of the $k$ sub-element of the $j$ element, $\delta S_{jk}$ is the surface of the $k$ sub-element and $N_{sub}$ is the number of internal subdivisions of each mesh element. The matrix formulation of Eq. 10 doesn't change with the implementation of our method,

maintaining constant the size of the original linear system. In this way, the computational cost and the size of computer memory that is needed for running these calculations is unchanged. The only impact, in terms of CPU operations, concerns the generation of $C$ and $B$ matrices, that will depend on $N_{sub}$.

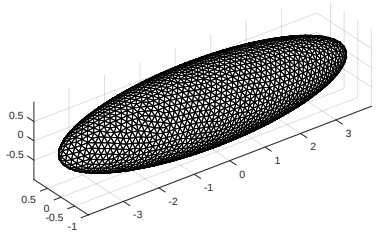


Figure 1: Triangular mesh of an ellipsoid

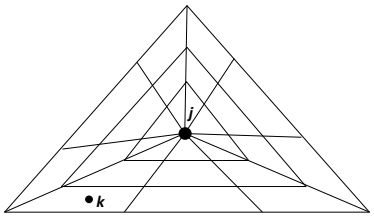


Figure 2: Subdivision of the $j$ element into $k$ sub-elements

### *2.4. Multiple Bodies*

The additional novelty proposed in this paper concerns the possibility to implement the method described in the previous sections to study the Added Masses of generic bodies in the presence of external objects or surfaces.

The case of a body-wall interaction is presented below. The effects of the flat wall can be computed by a discretization of its surface, or modeling it with the Image Method. In the first case, Eq. 10 is rewritten as:

$$[2\pi\mathbb{I}-C]_{(N_b+N_w)\times(N_b+N_w)}\{\varphi_i\}_{(N_b+N_w)\times 1} = -[B]_{(N_b+N_w)\times(N_b+N_w)} \left\{ \left. \frac{\partial \varphi_i}{\partial \vec{n}} \right|_{S_b+S_w} \right\}_{(N_b+N_w)\times 1} \tag{17}$$

where $N_w$ represents the number of discretization elements of the wall. The fundamental step to solve the problem is the correct definition of the boundary

conditions $\frac{\partial \varphi_i}{\partial \vec{n}}\big|_{S_b+S_w}$, which are imposed by the motions of the body and the wall. In the case of a fixed wall, therefore with a surface that has no velocities and no rotations, the six boundary conditions of each discretization point of the wall are equal to zero. So, for each elementary potential, the boundary conditions are:

$$\left\{ \frac{\partial \varphi_i}{\partial \vec{n}}\bigg|_{S_b+S_w} \right\}_{(N_b+N_w)\times 1} = \begin{bmatrix} \left\{ \frac{\partial \varphi_i}{\partial \vec{n}}\big|_{S_b} \right\}_{N_b\times 1} \\ \{0\}_{N_w\times 1} \end{bmatrix} \tag{18}$$

The evaluation of the Added Masses matrix is obtained from Eq. 11, with no modifications. It is important to underline that the local reference frame is unique and linked to the body center of volume.

The study of the wall presence by the Image Method is obtained by different modifications on the boundary conditions. In this case, Eq. 10 can be rewritten as:

$$[2\pi\mathbb{I}-C]_{(N_b+N_{im})\times(N_b+N_{im})}\{\varphi_k\}_{(N_b+N_{im})\times 1} = -[B]_{(N_b+N_{im})\times(N_b+N_{im})} \left\{ \frac{\partial \varphi_k}{\partial \vec{n}}\bigg|_{S_b+S_{im}} \right\}_{(N_b+N_{im})\times 1} \tag{19}$$

where $N_{im}$ is the number of elements of the image body. The boundary conditions depend on the reflected movement of the image body, so:

$$\left\{ \frac{\partial \varphi_k}{\partial \vec{n}}\bigg|_{S_b+S_{im}} \right\}_{(N_b+N_{im})\times 1} = \begin{bmatrix} \left\{ \frac{\partial \varphi_k}{\partial \vec{n}}\big|_{S_b} \right\}_{N_b\times 1} \\ \left\{ \frac{\partial \varphi_k}{\partial \vec{n}}\big|_{S_{im}} \right\}_{N_{im}\times 1} \end{bmatrix} \tag{20}$$

and, for example, when the wall is positioned orthogonally to the $z$ axis of the first body, the boundary conditions of the image body are:

$$\frac{\partial \varphi_k}{\partial \vec{n}}\bigg|_{S_{im}} = \begin{cases} \alpha & k=1 \\ \beta & k=2 \\ -\gamma & k=3 \\ -(d_y\gamma - d_z\beta) & k=4 \\ -(d_z\alpha - d_x\gamma) & k=5 \\ d_x\beta - d_y\alpha & k=6 \end{cases} \tag{21}$$

The negative signs depend on the fact that when the body moves in the positive direction of $z$ axis, its image moves in the opposite direction, and when it rotates

in the positive sense of the $x$ and $y$ axes, the rotation of the image along the same axes is negative.

## 3. Results

### *3.1. Validation of the method and mesh-sensitivity study*

In this section the validity of the method is studied by applying it to simple cases whose results are known.

Firstly, the analysis on a sphere, placed in infinite fluid, is presented. In this case the AM matrix is composed of three terms: $\lambda_{11}$, $\lambda_{22}$, $\lambda_{33}$. The theoretical values are:

$$\lambda_s = \lambda_{11} = \lambda_{22} = \lambda_{33} = \frac{2}{3}\rho\pi R^3 \tag{22}$$

where $R$ is the radius of the sphere. In this paper, the results are presented by the adimensional values $\lambda'$, obtained by dividing the Added Mass by the total mass of the fluid displaced by the sphere, $M_f$, that is the mass of fluid that would fill in the volume of the body. For a sphere this value is:

$$\lambda'_s = \frac{\lambda_s}{M_f} = \frac{\frac{2}{3}\rho\pi R^3}{\frac{4}{3}\rho\pi R^3} = \frac{1}{2} \tag{23}$$

Numerical results depend on the level of discretization of the body surface mesh and on the number of internal subdivision of its elements. Figure 3 shows an example of a mesh element with 27 internal subdivisions. Each edge of the triangle is split into $N_\theta$ divisions. Radially, from the centroid of the element, there are $N_r$ divisions.

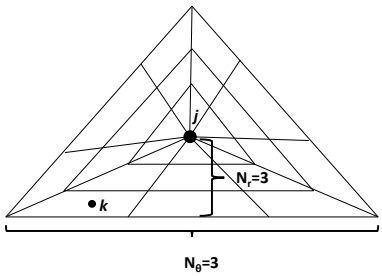


Figure 3: Subdivision of the element into 27 sub-elements, with $N_\theta = 3$ and $N_r = 3$

To understand the dependence of the mesh on the results, a parametric study on $N_\theta$, $N_r$ and $N_b$ is realized. Figure 4 shows the variation of the sphere AM (equal results are obtained on $\lambda'_{11}$, $\lambda'_{22}$ and $\lambda'_{33}$ thorough an uniform triangular surface mesh) as a function of $N_\theta$, discretized by $N_b = 2624$ elements and $N_r = 10$ radial subdivisions.

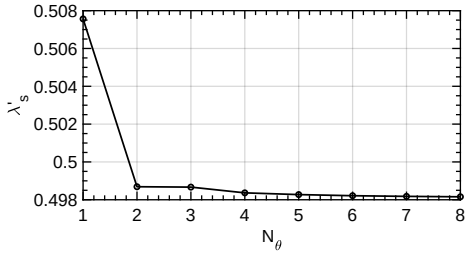


Figure 4: Added mass of the sphere as a function of $N_\theta$.

When $N_\theta = 1$ there is an overestimation of the AM value (in the theoretical case $\lambda'_s = 0.5$) and with $N_\theta \geq 2$ a smooth and stable evolution is found. From the last result, the parameter $N_\theta = 2$ is chosen for the rest of our analysis.

Figure 5 shows the influence of $N_r$ on a configuration when $N_\theta = 2$ and $N_b = 2624$.

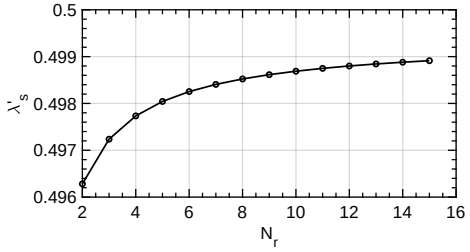


Figure 5: Added mass of the sphere as a function of $N_r$.

As might be expected, a greater discretization along the radial direction of the element ensures a better quality of the results. For the next analysis the value $N_r$ is fixed to 10, to guarantee a compromise in terms of quality of results and computational cost.

Finally, in Figure 6(a) it is shown the variation of the AM as a function of

the number of elements of the sphere mesh, $N_b$. A better discretization of the surface of the body determines a better estimate of the Added Masses. The relative error, calculated with respect to the theoretical value $\lambda'_s = 0.5$, shown in the graph of Figure 6(b), is very low, less than 0.5% for values of $N_b > 1400$.

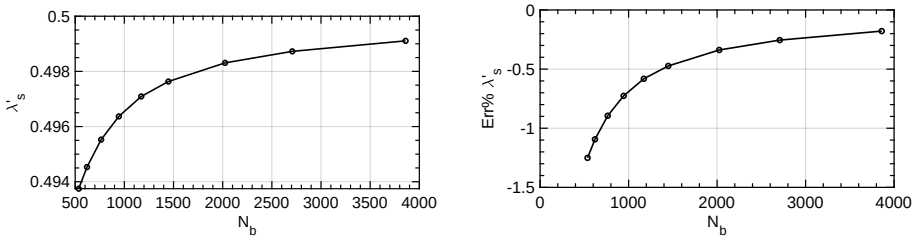


(a) (b)

Figure 6: Added mass and relative error of the sphere as a function of $N_b$.

Figure 7 shows the comparison between the error committed on the calculation of the AM and the error due to the discretization of the sphere surface with respect to its theoretical value, $S = 4\pi R^2$. The two curves show the same trend and the respective values are very similar. This highlights the direct dependence of the level of the mesh discretization and the quality of the numerical results.

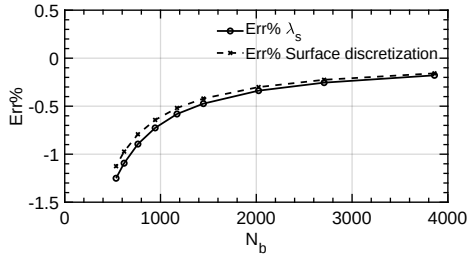


Figure 7: Comparison of the relative error in the calculation of the AM with the level of discretization of the sphere surface.

The second case analyzed concerns an ellipsoid of revolution whose axes ratio is $a/b = 3$ and $c/b = 1$, according to the scheme in Figure 8.

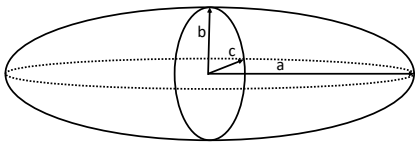


Figure 8: Scheme of an ellipsoid.

120 In this case, the theoretical AM can be evaluated by the following equations [2]:

$$\lambda_{11} = \frac{4}{3}\pi\rho abc\frac{A_0}{2 - A_0} \tag{24}$$

$$\lambda_{22} = \lambda_{33} = \frac{4}{3}\pi\rho abc\frac{B_0}{2 - B_0} \tag{25}$$

$$\lambda_{44} = 0 \tag{26}$$

$$\lambda_{55} = \lambda_{66} = \frac{4}{15}\pi\rho abc\frac{(a^2 - b^2)^2(A_0 - B_0)}{2(b^2 - a^2) + (B_0 - A_0)(b^2 + a^2)} \tag{27}$$

with:

$$A_0 = \frac{2(1 - e^2)}{e^3}\left[\frac{1}{2}\ln\frac{(1 + e)}{1 - e} - e\right] \tag{28}$$

$$B_0 = C_0 = \frac{1}{e^2} - \frac{1 - e^2}{2e^3}\ln\frac{1 + e}{1 - e} \tag{29}$$

$$e = \sqrt{1 - \frac{b^2}{a^2}} \tag{30}$$

Dimensionless mass terms of the AM matrix are obtained dividing $\lambda_{ii}$ $(i = 1, 2, 3)$ by:

$$M_f = \frac{4}{3}\pi\rho abc \tag{31}$$

and the inertia terms ($\lambda_{ii}$ with $i = 4, 5, 6$) by the body moments of inertia, respectively:

$$J_{xx} = \frac{4}{15}\pi\rho abc(b^2 + c^2) \tag{32}$$

$$J_{yy} = \frac{4}{15}\pi\rho abc(a^2 + c^2) \tag{33}$$

$$J_{zz} = \frac{4}{15}\pi\rho abc(a^2 + b^2) \tag{34}$$

The same analyses, carried out in the sphere case, are reproposed. The graphics in Figure 9 show the dependence of AM to $N_\theta$. For this analysis the parameters $N_r = 10$ and $N_b = 2428$ are adopted. As previously, the $N_\theta = 1$ case must be avoided, while $N_\theta \geq 2$ provides much more consistent results. The parameter $N_\theta = 2$ is chosen for the next investigation.

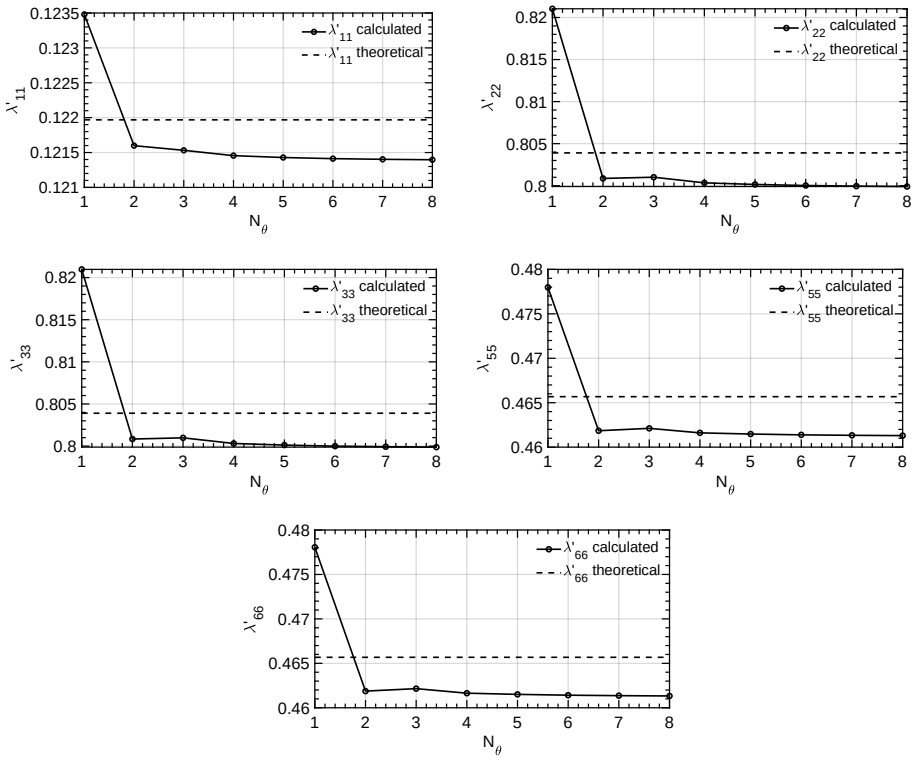


Figure 9: Added masses of the ellipsoid as a function of $N_\theta$.

Figure 10 shows the variation of AM as a function of $N_r$. The quality of results improves by increasing the number of $N_r$ divisions. As before, an excellent compromise, in terms of quality of results and computational cost, is obtained by $N_r = 10$.

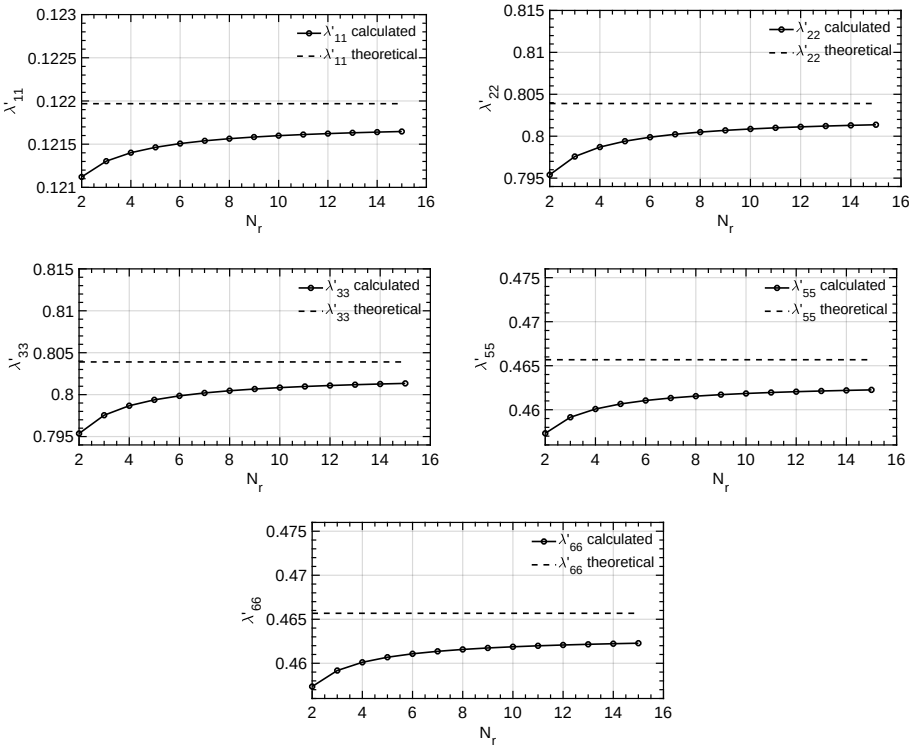


Figure 10: Added masses of the ellipsoid as a function of $N_r$.

In Figure 11 the variation of AM as a function of $N_b$ is presented.

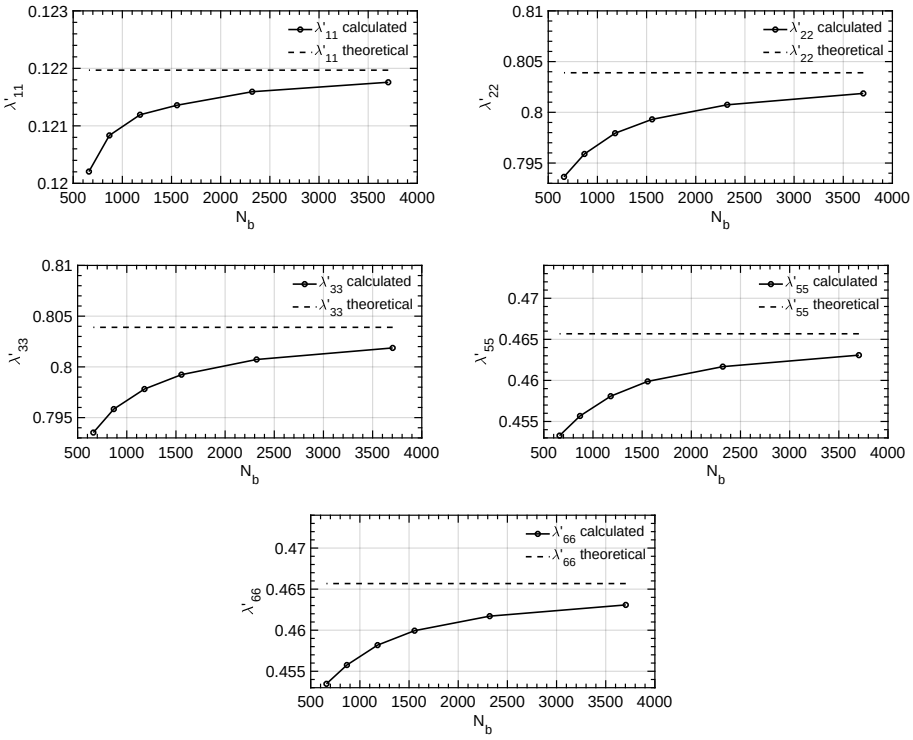


Figure 11: Added masses of the ellipsoid as a function of $N_b$.

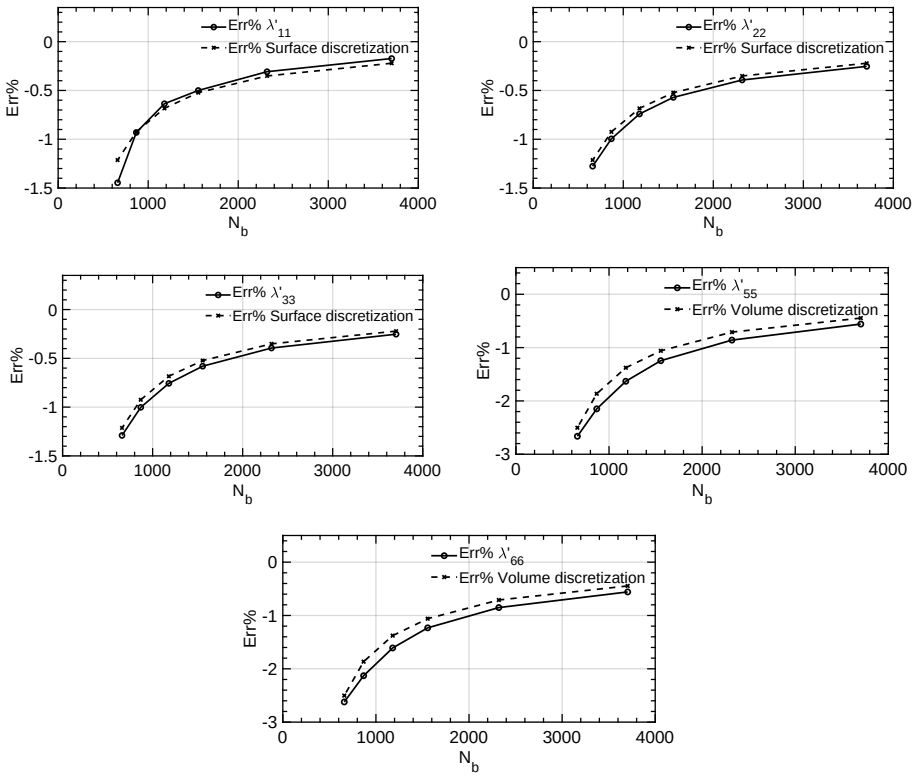


Figure 12: Relative error of ellipsoid AM as a function of $N_b$.

Graphs in Figure 12 show that the relative error committed on the calculation of $\lambda'_{ii}$, with $i = 1, 2, 3$, is very low and it is similar to the error committed on the surface discretization. The absolute value of the relative error for $\lambda'_{ii}$, with $i = 4, 5$, shows the same sensitivity of inertia terms to the volume discretization.

In the analyzed case, the error calculated on all AM values, with $N_\theta = 2$, $N_r = 10$ and $N_b \geq 2000$, is less than $-1\%$ and it depends only on the error committed on the surface and volume discretizations compared to the respective theoretical values.

To complete these analyses, in Figure 13 are shown the graphics representing the computational time required for a simulation as a function of $N_\theta$, $N_r$ and $N_b$. Numerical simulations are carried out on a laptop computer with an Intel Core i7-8550U and 16GB of RAM memory.

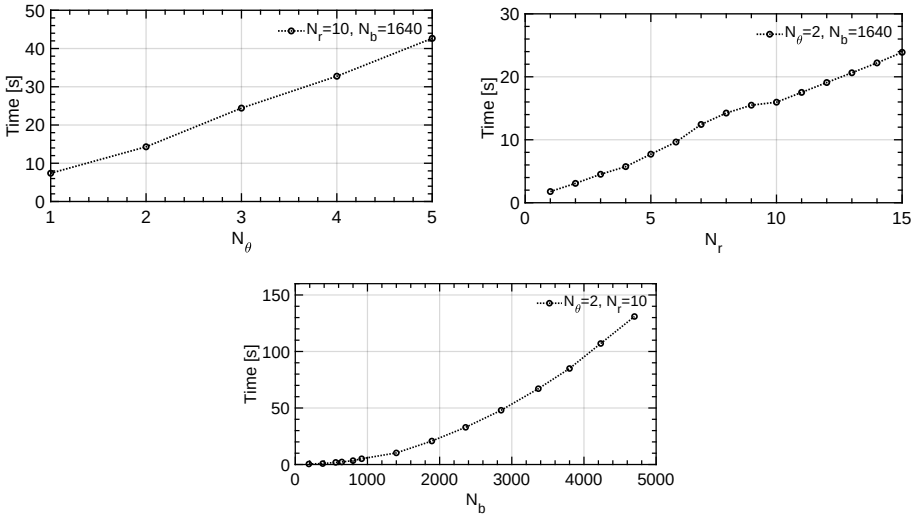


Figure 13: Simulation time as a function of $N_\theta$, $N_r$ and $N_b$.

The first two graphics show that the simulation time is a linear function of $N_\theta$ and $N_r$, because of the "for-loop" used for the generation of $C$ and $B$ matrices. In the last graphic, time is a function of $N_b^2$, because of the matrix inversion required to solve the linear system of equation 10.

*3.2. Sphere near a Flat Wall*

Here, the Added Masses matrix of a sphere, in the presence of a flat wall, is evaluated. The distance $h$, measured between the sphere center of volume and the wall is varied from $h = R$ to $h = 8R$. The comparison of two different simulation methods of the wall vicinity influence are analyzed. Firstly, a simulation is realized by direct discretization of the wall, as showed in Figure 14, with a circular surface of extension $S_w = \pi(20R)^2$. Secondly, by the Image Method, as it is shown in the scheme of Figure 15. To have a better representation of the relative variation of the AM, results are presented normalized by their simulated infinite-values.

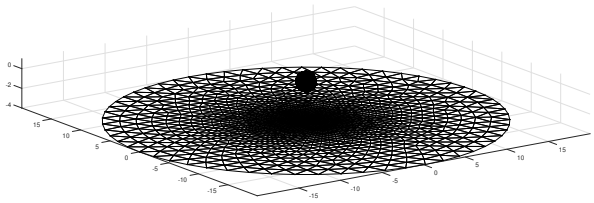

Figure 14: Discretization of a Flat Wall for the calculation of Added Masses.

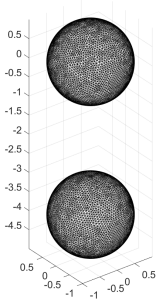

Figure 15: Modeling of a Flat Wall by the Image Method.

The number of elements chosen for the discretization of the sphere is $N_b = 2624$. The wall is discretized with 2876 elements. For the latter, the size of the mesh elements is variable, going from the size of a sphere element in the closest region to the body, to a larger size as one moves away from this point.

The parameters chosen for the internal subdivisions of each element are $N_\theta = 2$ and $N_r = 10$. Simulation results, performed in the two cases, are presented in Figure 16. These are compared to the results obtained by Kharlamov [5] and Korotkin [13].

Added Masses variations are equivalent in the two parallel directions to the wall ($\lambda'_{11}$ and $\lambda'_{22}$). The variation of $\lambda'_{33}$ (orthogonal direction) is more important when the sphere approaches the wall. The influence of the latter becomes negligible from six *radii*, where the Added Masses variation is less than 0.2% if compared to the infinite-value. From the last analysis it is possible to assume that the edge effects of the wall are limited to the range of influence of the wall on the body. So, in this case, a wall extension of $S_w = \pi(6R)^2$, considering $6R$ as the distance of the wall influence, is sufficient to achieve a good accuracy for our calculations.

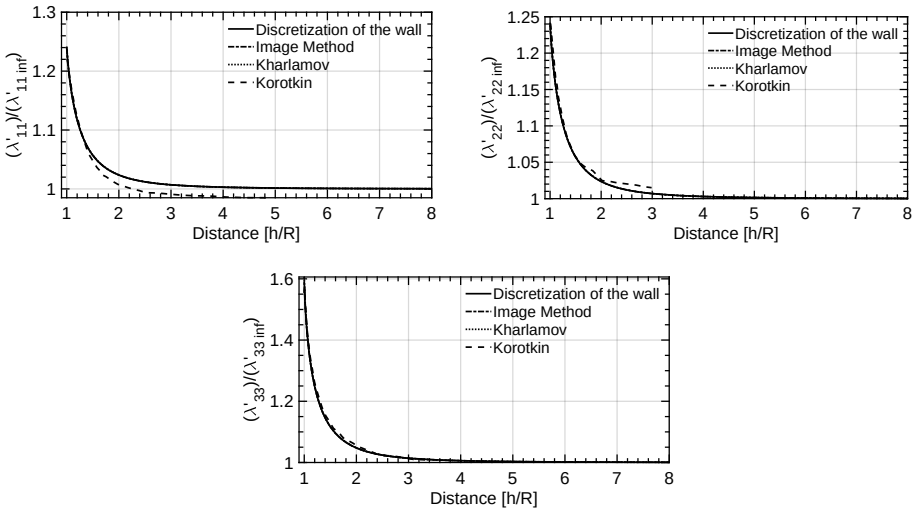


Figure 16: Sphere Added Masses variation as a function of the distance with the Wall.

There are not evident differences between the curves of our simulations and Kharlamov's results, for each $\lambda'_{ii}/\lambda'_{ii\,inf}$ considered. Korotkin's values seem to deviate slightly from ours and Kharlamov's ones, so they will not be further considered for the next analyzes. In the area $h/R < 1.5$, represented in Figure 17, some minimal discrepancies are evident between the results obtained by the discretization of the wall and by the Image Method. In particular, for $\lambda'_{33}/\lambda'_{33\,inf}$, a little deviation of the curve is observable when $h/R = 1$.

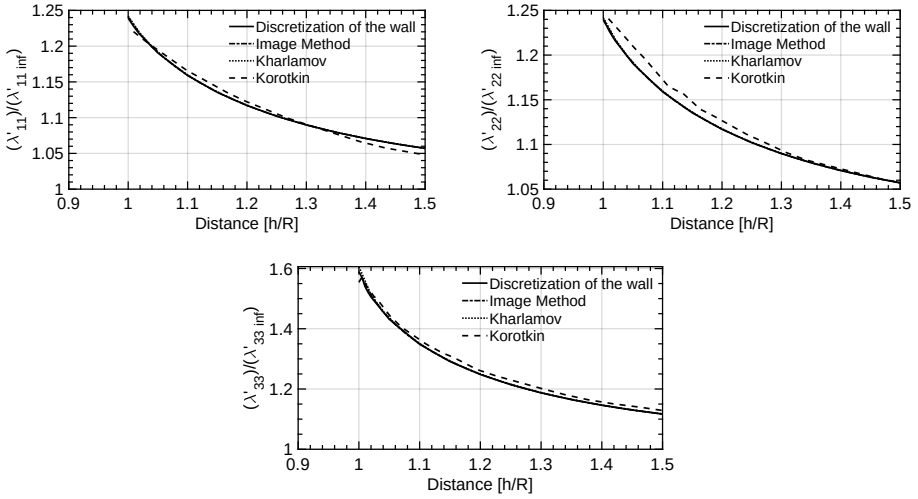


Figure 17: Added Masses variation in the near-wall area.

To quantify the accuracy of our methods, the root mean square of the error is evaluated in the considered domain ($1 \leq h/R \leq 8$), comparing our and Kharlamov's results. These values are presented in Table 1.

| RMS error | $\frac{\lambda'_{11}}{\lambda'_{11\,inf}}$ | $\frac{\lambda'_{22}}{\lambda'_{22\,inf}}$ | $\frac{\lambda'_{33}}{\lambda'_{33\,inf}}$ |
|---|---|---|---|
| Wall discretization - Kharlamov | 7.8895e-04 | 7.0915e-04 | 7.3847e-03 |
| Image Method - Kharlamov | 2.9811e-04 | 2.9811e-04 | 2.1911e-03 |

Table 1: Root Mean Square of the error for the three relative values of AM.

A further analysis consists in comparing the simulated AM to the existent theoretical values, when the sphere and the wall are in contact ($h/R = 1$). The

solutions found by Davis [4] ($\lambda'_{11} = \lambda'_{22} = 0.621$) and Hicks [3] ($\lambda'_{33} = 0.803085$) are the references. Results are presented in Table 2.

| $\frac{\lambda'_{ii}}{\lambda'_{ii\,inf}}\left(\frac{h}{R}=1\right)$ | $\frac{\lambda'_{11}}{\lambda'_{11\,inf}}$ | $\frac{\lambda'_{22}}{\lambda'_{22\,inf}}$ | $\frac{\lambda'_{33}}{\lambda'_{33\,inf}}$ |
|---|---|---|---|
| Wall discretization | 1.2389 | 1.2391 | 1.5540 |
| Image Method | 1.2406 | 1.2406 | 1.5900 |

Table 2: Relative AM variation in the contact condition.

Multiplying by the theoretical infinite-value $\lambda'_{ii\,inf} = 0.5$, the relative error with respect to the Davis and Hicks' values is obtained, as presented in Table 3.

| Err% $\left(\frac{h}{R}=1\right)$ | $\lambda'_{11}$ | $\lambda'_{22}$ | $\lambda'_{33}$ |
|---|---|---|---|
| Wall discretization | -0.2463 | -0.2359 | -3.2469 |
| Image Method | -0.1105 | -0.1096 | -1.0097 |

Table 3: AM error in the contact condition.

As already noted above, the larger error is committed on $\lambda'_{33}$ through the discretization of the wall. However, it is clear from the graphs in Figure 17 that only the contact point seems to be ambiguous. The problem can be due to the discretization of the sphere mesh, since some points of the latter could penetrate the wall, generating numerical aberrations.

With the considered sphere and wall meshes, the method give very satisfying results. Avoiding the contact point between the body and the wall, the error between our simulations and the theoretical references is very low, less than 1%.

In addition, a study on the mesh sensitivity is carried out. Figure 18 shows the relative error of four simulations, realized using the Image Method on a sphere with an increasing number of discretization elements $N_b$. The results are compared to those of Kharlamov. The equation for the calculation of the error is:

$$Err\% \frac{\lambda'_{ii}}{\lambda'_{ii\,inf}} = 100 * \left( \frac{\frac{\lambda'_{ii}}{\lambda'_{ii\,inf}}}{\frac{\lambda'_{ii\,Kharlamov}}{\lambda'_{ii\,inf\,th}}} - 1 \right) \tag{35}$$

The graphs show that the absolute value of the error increases by reducing the number of mesh elements. The maximum difference between the theoretical values and those of the simulations is observed when $h/R = 1$. At this position, the error committed on $\lambda'_{33}/\lambda'_{33\,inf}$ is $-1.9\%$ with a mesh of 764 elements. However, with the same mesh, the error is reduced to $-0.55\%$ when $h/R = 1.05$. Therefore avoiding only the point of contact between wall and sphere, the maximum error committed by our simulations is very low even with a very coarse surface discretization.

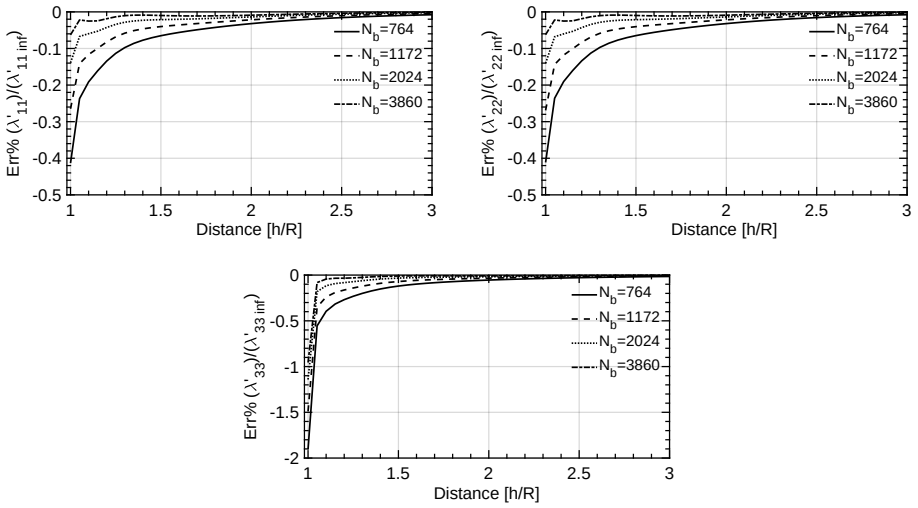


Figure 18: Mesh sensitivity on the Added Masses variations by the Image Method. Relative error evaluated from the Kharlamov's results.

The same mesh-sensitivity analysis is carried out on the results obtained through the wall discretization method. In this case, the sphere and wall meshes change at the same time. The same elements size for the two meshes is imposed (concerning the wall, we refer to the closest wall region to the sphere). The error, calculated as before, is represented in Figure 19. The number of elements $N_b$ on the graphs is referred to the sphere mesh. The values corresponding to the contact point have not been considered, because the error evaluated in the simulations with the coarsest mesh is quite high. On the other hand, the error evaluated on the rest of the domain is limited to $-1\%$.

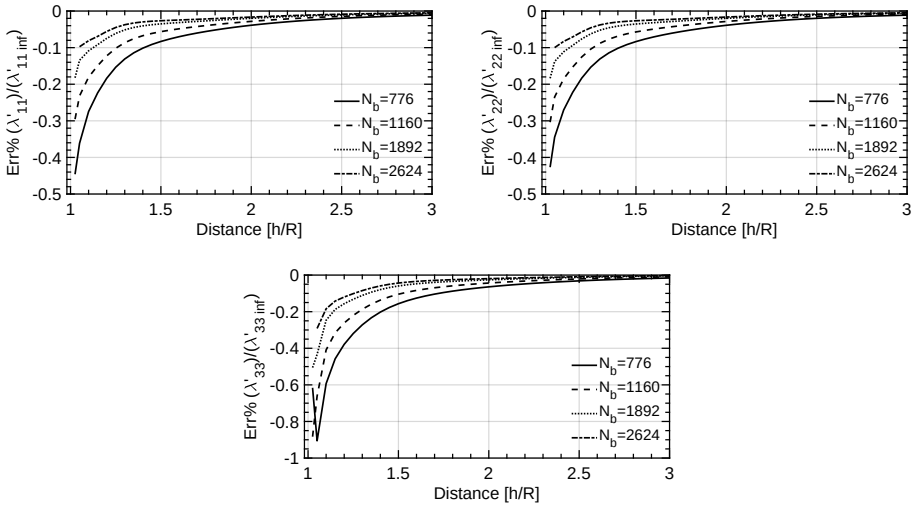


Figure 19: Mesh sensitivity on the Added Masses variations by the discretization of the wall. Relative error evaluated from the Kharlamov's results.

Finally, we can state that it is possible to estimate with good accuracy the relative variation of the AM with respect to the infinite value, even with a coarse mesh. Consequently, knowing the analytical infinite value, or calculating it with high precision, the associated absolute values is obtained with an error from the theoretical value lower than 1%.

*3.3. Ellipsoids near a Flat Wall*

In the following section, results of the numerical simulations, realized on ellipsoidal shapes with different combinations of the axes ratios $a/b$ and $c/b$ (referring to the ellipsoid in Figure 8), are presented. In this case, only the Image Method is adopted. The wall is parallel to the longitudinal axis of the ellipsoid. The reference frame is fixed on the body center of volume, with the $z$-axis directed towards the wall.

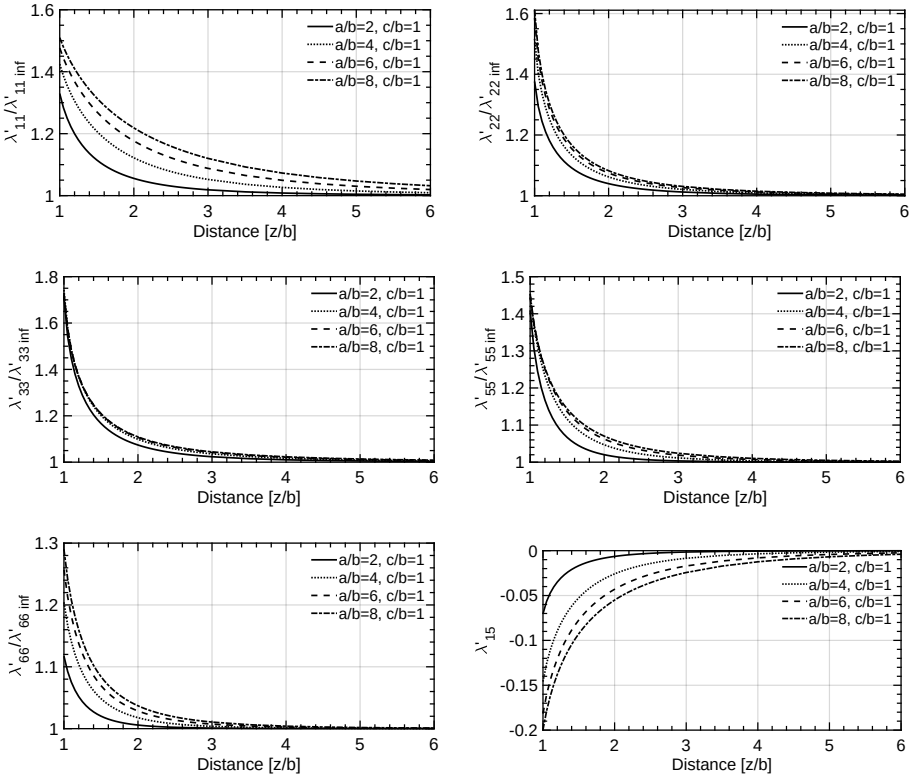


Figure 20: Variation of the AM on ellipsoids with axes ratios $c/b = 1$ as a function of the distance with a flat wall.

The graphs of Figure 20 show the Added Masses variations of ellipsoids with axes ratio $c/b = 1$. In the last graph it is shown the AM value $\lambda'_{15}$. This

adimensional value is obtained by:

$$\lambda'_{15} = \frac{\lambda_{15}}{\frac{4}{3}\pi a b^2 c} = \frac{\lambda_{15}}{M_f\, b} \tag{36}$$

This term of the AM matrix is not present when the ellipsoids are immersed in infinite fluid.

The last results suggest that the presence of the wall induces both an increase of all Added Mass values, and the emergence of new off-diagonal terms.

In Figure 21 and Figure 22 are shown the results obtained on ellipsoids with axes ratios $c/b = 2$ and $c/b = 3$. The increase in the axes ratios determines a larger variation on the AM, especially in the near wall area. In addition to $\lambda'_{15}$, the $\lambda'_{24}$ term appears when a scalene ellipsoids ($a \neq b \neq c$) is in the vicinity of the wall. The dimensionless value is obtained from the equation:

$$\lambda'_{24} = \frac{\lambda_{24}}{\frac{4}{3}\pi a b^2 c} = \frac{\lambda_{24}}{M_f\, b} \tag{37}$$

The last analysis helps better the understanding on how the presence of external walls has an impact on the Added Masses matrix. The take-off and landing are the most sensitive flight phases to these AM variations. Consequently, these results can not be neglected in the implementation of an aerodynamic model.

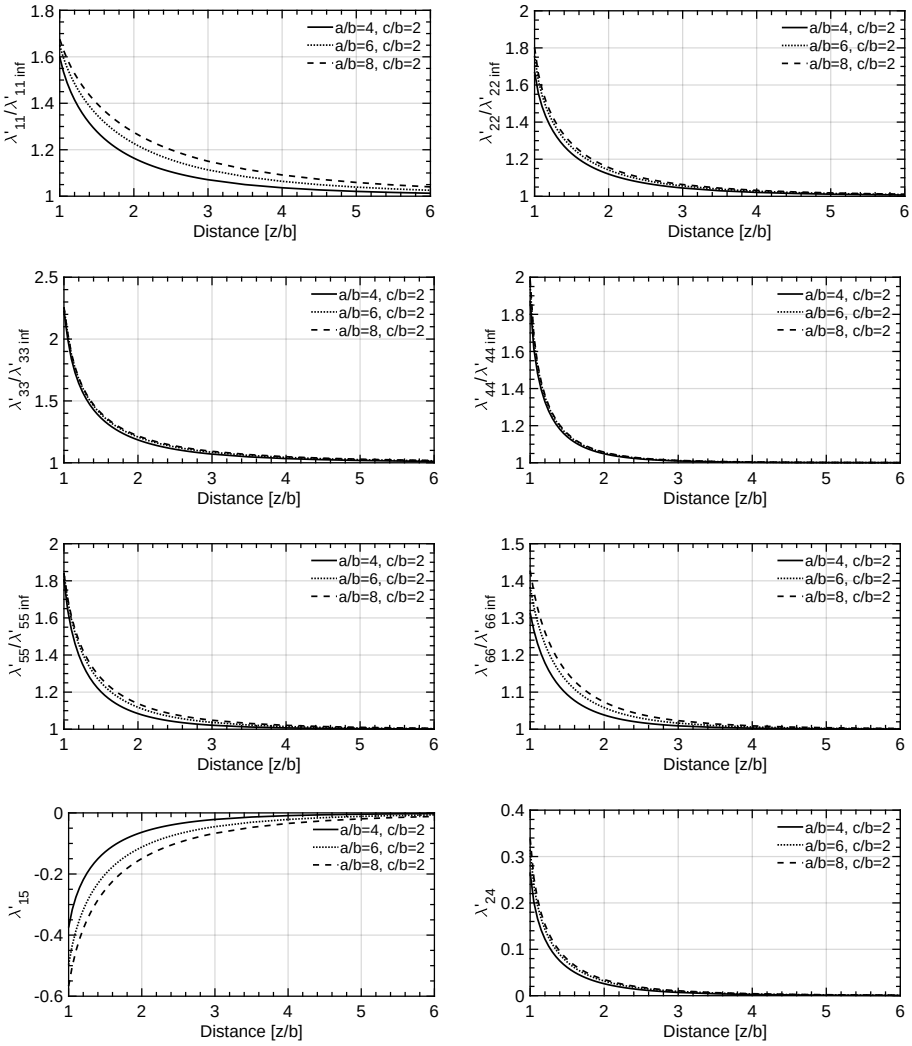


Figure 21: Variation of the AM on ellipsoids with axes ratios $c/b = 2$ as a function of the distance with a flat wall.

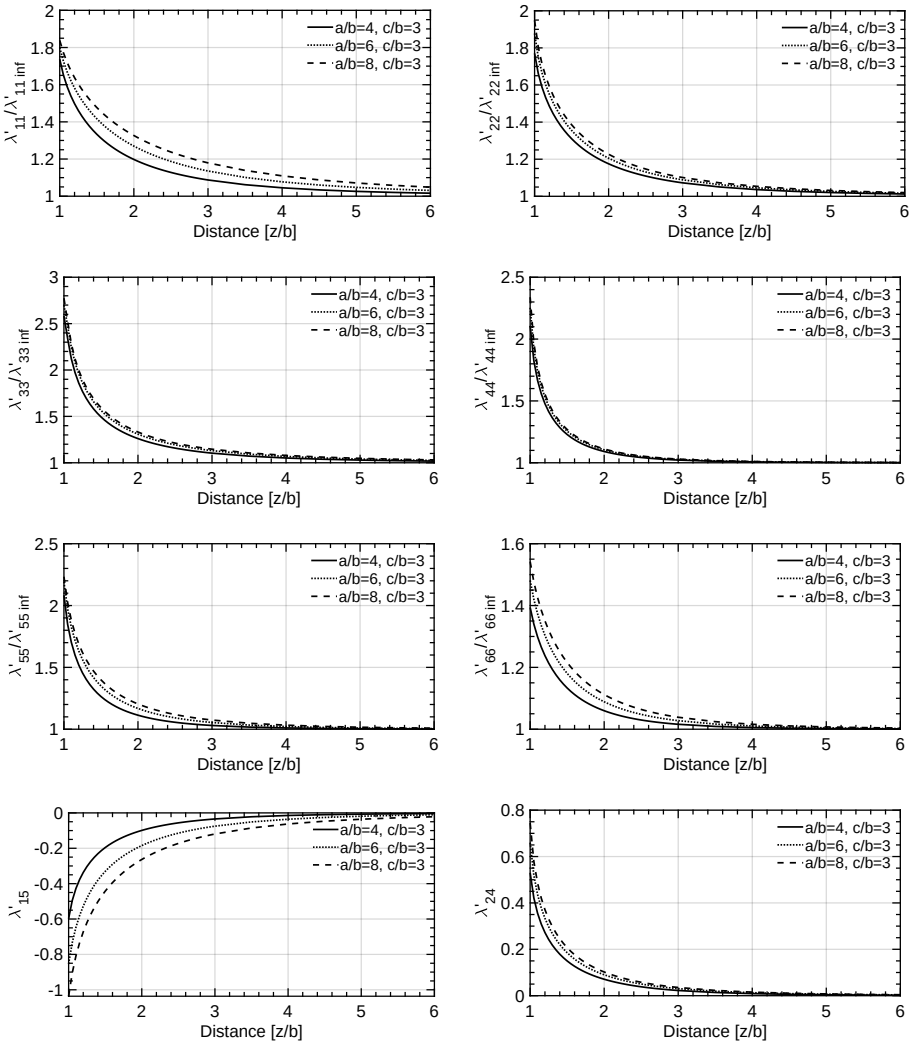


Figure 22: Variation of the AM on ellipsoids with axes ratios $c/b = 3$ as a function of the distance with a flat wall.

As in the sphere case, a study on the influence of the mesh on results is carried out. Simulations on an ellipsoid of revolution with axes ratios $a/b = 3$ and $c/b = 1$, are realized through the Image Method. Results of a configuration with $N_b = 2916$ are compared to Korotkin's [13] results, as shown in Figure 23.

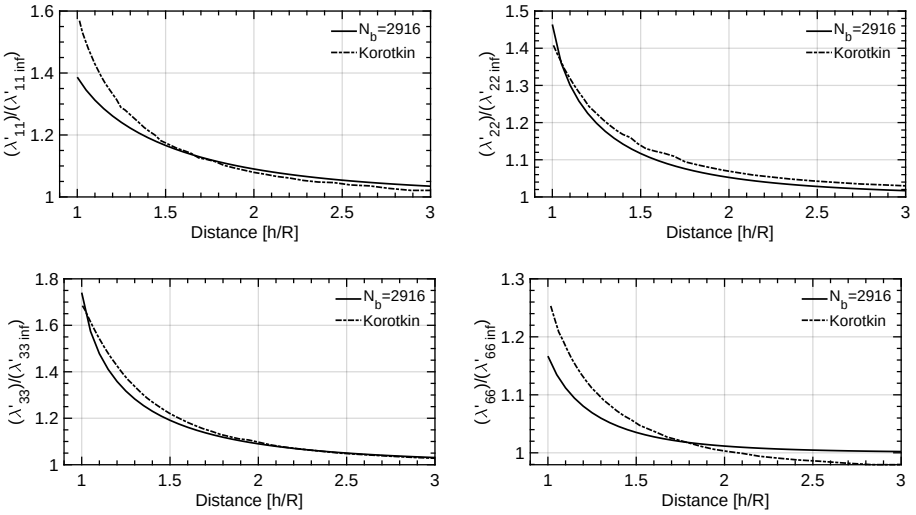


Figure 23: Ellipsoid Added Masses variation as a function of the distance with the Wall.

From the graphs it is possible to see marked differences in all AM curves. Furthermore, Korotkin's results seem incomplete, since there is no reference to $\lambda'_{55}$ and $\lambda'_{15}$ terms. For these reasons and for the doubts already arisen in the sphere case, the results of Korotkin will not be further considered for the analysis of the error.

In Figure 24, the influence of the mesh has been studied comparing the ellipsoid discretized with a number of elements $N_b = 2916$ to coarser meshes. The relative error is calculated according to the following equation:

$$Err\% \frac{\lambda'_{ii}}{\lambda'_{ii\,inf}} = 100 * \left( \frac{\frac{\lambda'_{ii}}{\lambda'_{ii\,inf}}}{\frac{\lambda'_{ii\,N_b=2916}}{\lambda'_{ii\,inf\,N_b=2916}}} - 1 \right) \tag{38}$$

Also in this case, with less detailed meshes there is an underestimation of the AM variations.

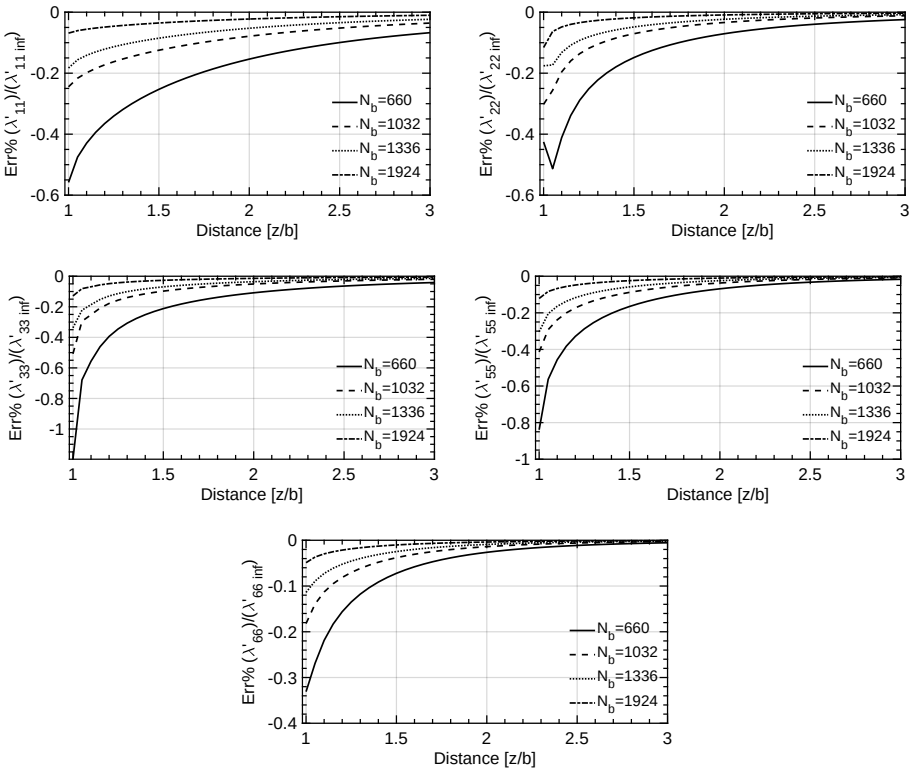


Figure 24: Mesh sensitivity on the Added Masses variations of an ellipsoid.

The maximum relative error is obtained when the body and the wall are in contact. For $\frac{\lambda'_{33}}{\lambda'_{33\,inf}}$, the error in this position is about $-1.2\%$ with a mesh that has a number of elements five times smaller than the reference.

The mesh-sensitivity studies conducted on the sphere and on the ellipsoid give the same tendencies. To ensure a very good quality of the results, so with $-0.2\% < Err\% < 0\%$, it's suggested to use a mesh with $N_b > 2000$. To obtain results with an error $-1\% < Err\% < -0.2\%$, but with an inferior computational cost, it's recommended to use $700 < N_b < 2000$.

*3.4. Airship near a generic-shape wall*

The potentiality of our method concerns the possibility to calculate the AM on bodies in the vicinity of walls with generic shapes. Below, results of simulations carried out on an airship, discretized with a mesh of 5732 elements, in the presence of a possible mountain ground are presented. A representation of the configuration is shown in Figure 25. A better representation of the airship is shown in Figure 26. The dimensions of the airship are $3\,b$ for the longitudinal half-length, $2.2\,b$ for the lateral half-length and $b$ for the half height. The two mountains are modeled by a Gaussian distribution. The distance of their mean from the airship is $20b$.

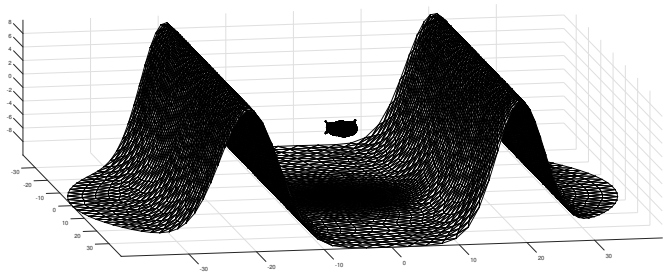

Figure 25: Discretization of the airship and of a mountain ground.

The simulated AM values of the airship in infinite fluid are :

$$\mathbb{M}'_a = \begin{bmatrix} 0.2034 & 0 & 0 & 0 & 0 & 0 \\ 0 & 0.3513 & 0 & 0 & 0 & -0.0141 \\ 0 & 0 & 1.4829 & 0 & 0.0479 & 0 \\ 0 & 0 & 0 & 0.5926 & 0 & 0 \\ 0 & 0 & 0.0479 & 0 & 0.7954 & 0 \\ 0 & -0.0141 & 0 & 0 & 0 & 0.0762 \end{bmatrix} \tag{39}$$

where $\lambda_{ii}$ with $i = 1, 2, 3$ are normalized by the mass of the airship, $\lambda_{ii}$ with $i = 4, 5, 6$ are normalized by the respective moments of inertia, $\lambda_{26}$ and $\lambda_{35}$ are

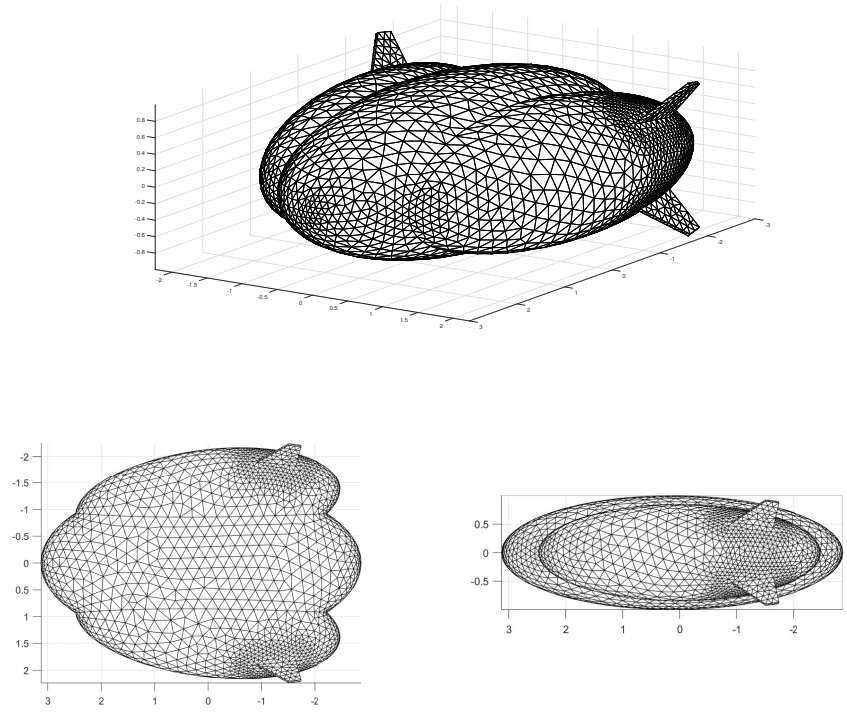

Figure 26: Discretization of the airship.

normalized by the mass of the airship multiplied by the cubic root of its volume. The graphs of Figure 27 show the relative variation of the added masses of the airship in the presence of the ground when the aircraft change its position in the vertical direction. For simplicity of representation, only the diagonal terms of the Added Masses matrix are presented.

A simulation of an ellipsoid with axes ratios $a/b = 3$ and $c/b = 2$ in the proximity of a flat wall is proposed to compare the results obtained on the airship.

In the closest area to the wall, $1 < z/b < 2$, the AM variations on the ellipsoid are greater than those observed on the airship. This is particularly evident in the graph of $\frac{\lambda'_{66}}{\lambda'_{66\,inf}}$. The last analysis highlights that the simulations realized on simplified shapes can lead to erroneous results in the near wall region

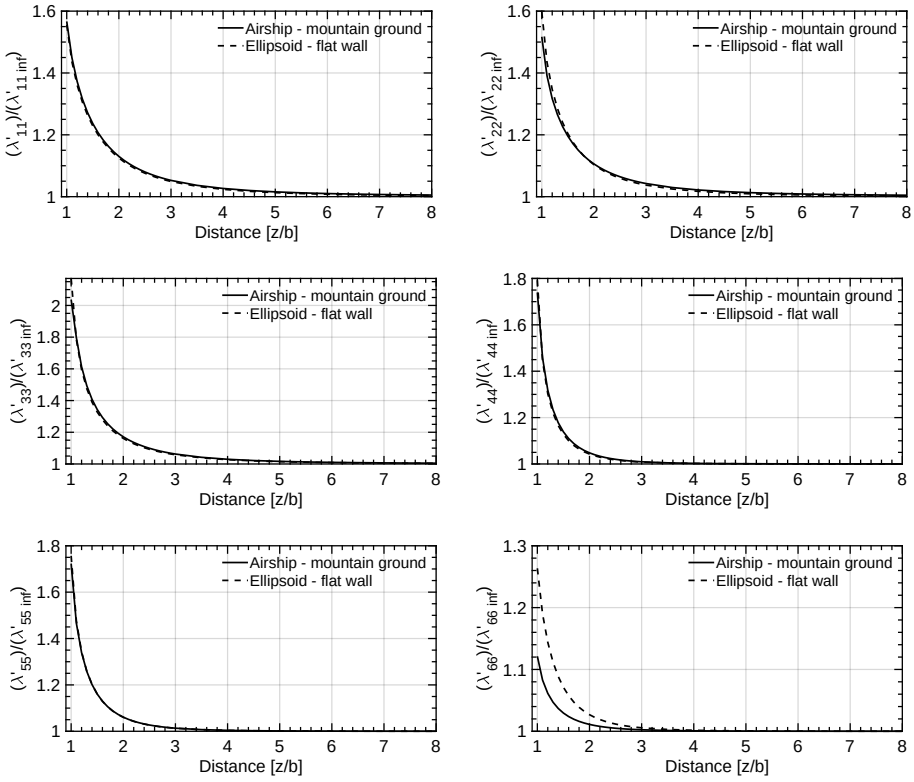


Figure 27: AM variations on an airship in the presence of a mountain ground and on an ellipsoid with axes ratios $a/b = 3$ and $c/b = 2$ in the presence of a flat wall.

with an overestimation of the AM. Calculations realized on the real shape are recommended to obtain more truthful results.

## 4. Conclusions

In this study the Boundary Element Method was adopted to determine the Added Masses of generic shape bodies interacting with external walls. Results of these analyses are fundamental for the airship dynamics, in particular to ensure the correct maneuverability and stability of the aircraft during operations in the proximity of the ground. The simulations carried out demonstrated that the quality of the numerical results depend on the mesh discretization level, as a function of the number of mesh elements and sub-elements. The cases of a sphere and of ellipsoids interacting with a flat wall are studied through the discretization of the wall surface and via the Image Method. In both cases, the results obtained are very satisfactory and in good agreement with the theoretical references. A mesh-sensibility study demonstrate that a number of elements $N_b = 1500$, with internal subdivisions of $N_\theta = 2$ and $N_r = 10$, can lead to the best compromise in terms of results quality and computational cost for ellipsoidal shapes. Finally, the study on an airship shows that the approximation of the body by the relative ellipsoidal shape lead to insufficient accurate results in the near-wall area, with the tendency to overestimate the AM variations.

## References


[1] P. L. G. Du Buat, Principes d'hydraulique et de pyrodynamique, vérifiés par un grand nombre d'expériences faites par ordre du gouvernement, Vol. 1, 1816.

[2] H. Lamb, Hydrodynamics, Cambridge university press, 1932.

[3] W. M. Hicks, Xiii. on the motion of two spheres in a fluid, Philosophical Transactions of the Royal Society of London (171) (1880) 455–492.

[4] A. Davis, High frequency limiting virtual-mass coefficients of heaving half-immersed spheres, Journal of Fluid Mechanics 80 (2) (1977) 305–319. doi:10.1017/s0022112077001694.

[5] A. A. Kharlamov, Z. Chára, P. Vlasák, Hydraulic formulae for the added masses of an impermeable sphere moving near a plane wall, Journal of Engineering Mathematics 62 (2) (2008) 161. doi:10.1007/s10665-007-9186-y.

[6] N. Azouz, S. Chaabani, J. Lerbet, A. Abichou, Computation of the Added Masses of an Unconventional Airship (2012). doi:10.1155/2012/714627.

[7] J. L. Hess, A. M. O. Smith, Calculation of potential flow about arbitrary bodies, Progress in Aerospace Sciences 8 (1967) 1–138. doi:10.1016/0376-0421(67)90003-6.

[8] L. Morino, C.-C. Kuot, Subsonic potential aerodynamics for complex configurations: a general theory, AIAA journal 12 (2) (1974) 191–197. doi:https://arc.aiaa.org/doi/abs/10.2514/3.49191.

[9] A. Ceruti, T. Bombardi, P. Marzocca, A CAD environment for the fast computation of Added Masses, Ocean Engineering 142 (2017) 329–337. doi:10.1016/j.oceaneng.2017.07.026.

[10] M. Tuveri, A. Ceruti, P. Marzocca, Added masses computation for unconventional airships and aerostats through geometric shape evaluation and meshing, International Journal of Aeronautical and Space Sciences 15 (3) (2014) 241–257. doi:10.5139/ijass.2014.15.3.241.

[11] H. Ghassemi, E. Yari, The added mass coefficient computation of sphere, ellipsoid and marine propellers using boundary element method, Polish Maritime Research 18 (1) (2011) 17–26. doi:10.2478/v10012-011-0003-1.

[12] A. Ceruti, D. Gambacorta, P. Marzocca, Unconventional hybrid airships design optimization accounting for added masses, Aerospace Science and Technology 72 (2018) 164–173. doi:10.1016/j.ast.2017.10.042.

[13] A. I. Korotkin, Added Masses of Ship Structures, Springer Netherlands, 2009. doi:10.1007/978-1-4020-9432-3.